

Coverage dependent desorption kinetics of CO from Rh(111) using time-resolved specular helium scattering

K. A. Peterlinz, T. J. Curtiss, and S. J. Sibener

The Department of Chemistry and the James Franck Institute, The University of Chicago, Chicago, Illinois 60637

(Received 12 June 1991; accepted 18 July 1991)

Linearized measurements of the coverage dependent desorption rates of CO from Rh(111) were made with a novel three molecular beam apparatus. To measure these isothermal and essentially isosteric rates we introduce a new *kinetic response amplifier*, namely time-resolved specular helium scattering, which makes use of the large attenuation cross section that CO has for specular helium scattering. The measurements are made by using one intense and continuous CO beam to establish a specific adsorbate coverage while another low intensity and chopped CO beam is used to weakly modulate the adsorbate density around the selected steady state. The transient helium reflectivity waveforms we measure during the modulated CO scattering contain the desired kinetic information, and are typically one to almost two orders of magnitude more sensitive to the desorption kinetics than are the signals arising from direct detection of desorbing CO. Desorption rates are reported for $0 < \theta_{CO} < 0.22$ and $440 \text{ K} < T_s < 555 \text{ K}$. He diffraction measurements revealed that the CO overlayer was disordered for all conditions for which kinetics were measured, and that the sticking coefficient varied with coverage as $S_0 (1 - 3\theta)$. At least a second order expansion of the chemical potential in terms of CO coverage was needed to explain these rates. The experimentally determined desorption rates can be fit equally well by placing the coverage dependence in either the pre-exponential factor or in the activation energy: $k(\theta, T_s) = 1.33 \times 10^{14} \exp[0.344\theta + 48.8\theta^2 - (32.3 \text{ kcal/mol})/(k_b T_s)] \text{ s}^{-1}$, or $k(\theta, T_s) = 1.33 \times 10^{14} \exp[-(32.3 - 1.62\theta - 38.3\theta^2 \text{ kcal/mol})/(k_b T_s)] \text{ s}^{-1}$. The measured He diffraction data, sticking coefficient, specular He scattering attenuation vs CO coverage, and increase in CO desorption rate with increasing coverage imply nearest-neighbor repulsive interactions. The use of time-resolved specular He scattering for studying coverage dependent reactions is also discussed.

I. INTRODUCTION

Although chemisorption on surfaces is dominated energetically by the adsorbate–surface interaction, interadsorbate interactions can cause dramatic changes in surface structure and adsorption–desorption kinetics as adsorbate coverage is increased.^{1,2} Modulated molecular beam methods have been utilized to a great extent in the past to study the kinetics and dynamics of low coverage single adsorbate systems. Reactive scattering experiments using single crystal surfaces have revealed much about the fundamental interactions between molecules and surfaces.³ Until recently, few molecular beam experiments have addressed high coverage systems where adsorbate interactions have significant effects on the kinetics and dynamics of the system.^{4–7}

Temperature programmed desorption (TPD)⁸ and isothermal desorption^{2,5,9} measurements of high coverage systems have demonstrated the dramatic effect that higher adsorbate coverages can have on desorption kinetics. Unfortunately, rapidly changing surface temperatures (T_s) and adsorbate coverages (θ) lead to measured desorption rates for irreversible desorption, not necessarily the equilibrium desorption rates. Steady state and equilibrium measurements,¹⁰ made with a constant incident gas flux density and constant surface temperature, have also revealed the strong coverage dependence of molecular desorption kinetics. However, extracting exact rates depends strongly on un-

confirmed assumptions about the coverage and temperature dependence of the molecular sticking coefficient at desorption temperatures. Detailed measurements of the coverage dependence of *equilibrium* desorption rates, as well as the coverage dependence of the sticking coefficient and adsorbate ordering, are necessary for understanding interadsorbate interactions^{11–14} and manifestations such as the compensation effect.¹⁵

Here we present a study of CO adsorption–desorption on Rh(111) which utilized a novel three molecular beam scattering technique. Incorporating modulated CO and He scattering, a highly sensitive *in situ* surface structure and coverage probe, we measured coverage dependent isothermal desorption rate constants for a range of well-defined CO coverages approaching $\frac{1}{2}$ monolayers (ML). By using three alternative methods of measurement and analysis, we confirmed these as isosteric desorption rate constants and confirmed the coverage dependence of the sticking coefficient. We also used He diffraction to establish the approximate order–disorder phase transition temperature for this adsorbate system.

The current study was motivated by two goals. The first was to develop the coverage perturbation technique for extracting kinetic information using time-resolved He scattering to probe coverages and kinetics. These techniques can then be extended to examine coverage dependent reactive systems (e.g., CO oxidation, hydrogen recombination, thin

film growth, etc.). The second was to increase our understanding of the coverage dependent desorption kinetics of CO on Rh(111), a system previously studied by Thiel *et al.*¹⁶ using conventional TPD methods.

The CO/Rh(111) system has been studied extensively in the past due to the important role rhodium plays as a primary component in automobile catalytic converters. It has also attracted attention since it supports the presence of two ordered phases of CO. At low coverages and temperatures, electron-energy-loss spectroscopy (EELS) work has shown that CO occupies top sites on the Rh(111) surface.¹⁷ Low-energy electron diffraction spectroscopy (LEED) has confirmed that, up to a coverage of $\frac{1}{3}$ ML, CO will occupy top sites and ultimately form a $(\sqrt{3} \times \sqrt{3})R30$ pattern.¹⁸ Above $\frac{1}{3}$ ML, CO will start to occupy twofold bridge sites, eventually converging to a (2×2) pattern of mixed, offset top and bridge sites¹⁶ at a saturation coverage of $\frac{4}{3}$ ML.^{19,20} Efforts have also been made, utilizing TPD, to establish the coverage dependent activation energies, pre-exponentials, and sticking coefficients.¹⁶ Although a significant change in kinetics as a function of coverage was measured, large uncertainties in the magnitude of the coverage dependent rate constants still exist.

Experimental modulated molecular beam techniques and methods of kinetics analysis in the zero coverage limit are well known.³ In contrast, only recently has work in our lab,^{21,22,23} as well as time-resolved EELS measurements,^{4,6} demonstrated that kinetic rate constants for complex nonlinear and coverage dependent reactions can be determined by measuring the relaxation rates for small coverage perturbations around a steady state coverage. Utilizing traditional single modulated molecular-beam techniques, we determined the near zero coverage rate constants for CO on Rh(111) by measuring the direct time-dependent desorption flux of modulated CO from Rh(111). Extensions of the single beam technique to higher coverages, equivalent to isothermal adsorption and desorption measurements, result in data that cannot be reliably analyzed for isosteric rate constants due to nonlinear effects.^{21,22,23} In order to determine accurate isosteric desorption rate constants, we used multiple beam techniques for higher coverage measurements.

The most straightforward way to determine higher coverage desorption rate constants is to use a high intensity, continuous beam to establish a steady state coverage and a low intensity, modulated beam to induce small coverage perturbations and collect a CO product waveform. However, there are several problems associated with collecting a product waveform for these higher coverages. Given a constant incident beam intensity, the steady state coverage increases as the rate constant is decreased by decreasing the surface temperature. As the rate constant decreases, though, the desorption flux will eventually become undetectable (i.e., the response is spread out over too long a time period to be detected in the usual way). Also, as the coverage increases, a significant portion of the incident beam is diffusely scattered into the detector and is difficult to separate from the desorbed flux. Clearly, direct desorption flux measurements are most informative in the low coverage regime.

Specular He scattering, however, is extremely sensitive

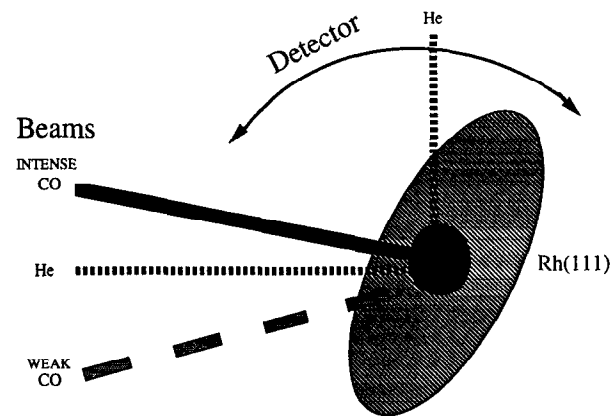


FIG. 1. Triple-beam arrangement for CO desorption measurements. One continuous, high intensity CO beam establishes a CO coverage at set T_s while a second, low intensity beam weakly modulates coverage. A third specularly scattered helium beam monitors changes in the CO coverage. The detector can be rotated to measure helium diffraction from the Rh(111) surface and the ordered CO overlayers.

to surface coverage, and can readily be used to amplify the response from changes in surface coverage over a wide coverage range. Poelsema and Comsa²⁴ have shown that, due to the large scattering cross section of adsorbates, the specular He signal is rapidly attenuated as coverage increases on low index surfaces. By carefully calibrating this attenuation as a function of adsorbate coverage, the specular helium scattering signal may be used to probe coverages directly. The high sensitivity of the resulting coverage measurements allows us to measure very small coverage modulations around a wide range of similarly measured steady state coverages. Utilizing the scheme outlined above, with the exception that, instead of measuring desorption flux, we directly measure coverage changes via He scattering due to a weak modulated CO beam (Fig. 1), we were able to linearize and measure the kinetic response to a weak intensity CO beam and, subsequently, extract rate constants at well-defined CO coverages. Since much of the kinetic analysis has been outlined in previous papers,^{4,10,21-23} we present here an overview of the three methods of measurements and analysis used to extract and confirm coverage dependent rate constants.

II. METHODS OF RATE-DATA ANALYSIS

A. Rates from steady state measurements

A gas in equilibrium with a surface can be described by the mass balance equation:

$$S(T_s, \theta)I = k(T_s, \theta)\theta, \quad (1)$$

where $S(T_s, \theta)$ is the temperature and coverage dependent sticking coefficient, I is the incident gas flux density, $k(T_s, \theta)$ is the temperature and coverage dependent desorption rate constant, and θ is the coverage of the gas on the surface, defined as the number of gas molecules per number of surface atoms. For CO on most noble metal surfaces, S is temperature independent and isotropic,³ so the temperature dependence is assumed to be negligible and will be dropped. Assuming a modified Langmuir form for the sticking coefficient below $\frac{1}{3}$ ML, the sticking coefficient can be expressed as

$$S(\theta) = S_0(1 - 3\theta), \text{ where } S_0 \equiv S(0). \quad (2)$$

We have confirmed the validity of this form for the temperature range $325 \text{ K} < T_s < 390 \text{ K}$ using thermal desorption calibration procedures discussed below (see Sec. V B).

When we establish a steady state coverage θ with beam flux density I , we extract $k(T_s, \theta)$ from Eqs. (1) and (2):

$$k(T_s, \theta) = \frac{S_0(1 - 3\theta)I}{\theta}. \quad (3)$$

If we can determine I , S_0 , and establish the form for the coverage dependence of the sticking coefficient, our He scattering measurements of the steady state coverages can be used to determine the isothermal, isosteric desorption rate constants.

B. Rates from modulated coverage and incident beam flux density measurements

The kinetic analysis for the linearized modulated beam experiment was recently formalized by Hinch and Dubois⁴ for the case of a pulsed molecular beam. Here we add the contribution of the weak time dependent incident beam flux density, $I(t)$, to the measured first-order desorption rate expression [see also Eqs. (7) and (8) of Ref. 4]:

$$\frac{d\Delta\theta(t)}{dt} = S(\theta_0)I(t) - k_m(T_s, \theta_0)\Delta\theta(t), \quad (4)$$

where θ_0 (θ_s in Ref. 4) and $\Delta\theta(t)$ are the steady state and weakly modulated surface coverages, respectively. $S(\theta_0)$ is the coverage dependent sticking coefficient at the steady state coverage, and $k_m(T, \theta_0)$ is the measured relaxation rate constant. In our experiment, we use a square wave modulation,

$$I(t) = \begin{cases} I_w & 0 < t < \tau \\ 0 & \tau < t < 2\tau \end{cases}, \quad (5)$$

for which 2τ is the modulation period, and I_w and I_s (σ_s in Ref. 4) are the weak and strong beam flux densities, respectively ($I_w \ll I_s$). Square wave modulation enables us to verify the linearity of the kinetics (as discussed below in Sec. III). Noting that $k_m(T_s, \theta_0)$ is not the true desorption rate constant $k(T_s, \theta_0)$, we can still obtain the true rate constant by allowing the perturbed coverage $\Delta\theta(t)$ to reach a steady state [i.e., $\tau \rightarrow 4/k_m(T_s, \theta_0)$].

In the steady state limit, Eq. (4) assumes the same form as Eq. (1):

$$S(\theta_0)I_w = k_m(T_s, \theta_0)\Delta\theta(\tau) \quad \lim \tau \rightarrow 4/k_m(T_s, \theta_0). \quad (6)$$

The desorption rate can be expressed independently of the sticking coefficient by dividing Eq. (6) by Eq. (1) and solving for $k(T_s, \theta_0)$:

$$k(T_s, \theta_0) = k_m(T_s, \theta_0) \frac{\Delta\theta(\tau)}{\theta_0} \frac{I_s}{I_w} \lim \tau \rightarrow 4/k_m(T_s, \theta_0). \quad (7)$$

Here we obtain a form for the rate constant that uses only the measured rate constant, the measured molecular-beam intensities, and the measured steady state and changing coverage. The only assumption is that the sticking coefficient depends only on coverage and temperature. However, the sticking coefficient may depend on the beam velocity and incident angle as well; in this experiment the incident angles for both CO beams were the same, and differences in beam velocities will be addressed later.

C. Rates from modulated coverage measurements, sticking coefficients known

If incident beam flux densities are not known, one can still give an explicit solution for all the first order contributions to k_m :

$$k_m(T_s, \theta_0) = \begin{cases} k(T_s, \theta_0) + \theta_0 \frac{dk(T_s, \theta)}{d\theta} \Big|_{\theta_0} - (I_s + I_w) \frac{dS(\theta)}{d\theta} \Big|_{\theta_0} & 0 < t < \tau \\ k(T_s, \theta_0) + \theta_0 \frac{dk(T_s, \theta)}{d\theta} \Big|_{\theta_0} - I_s \frac{dS(\theta)}{d\theta} \Big|_{\theta_0} & \tau < t < 2\tau \end{cases}, \quad (8)$$

which can be used to extract $k(T_s, \theta_0)$ from $k_m(T_s, \theta_0)$ (see also Ref. 4). As long as $I_w \ll I_s$, the second half solution can be used for both halves of the modulation period. From Eq. (1), we note $I_s = k(T_s, \theta_0)\theta_0/S(\theta_0)$, and, from Eq. (2),

$$\frac{dS(\theta)}{d\theta} \Big|_{\theta_0} = -3S_0. \quad (9)$$

These lead directly to a final solution for $k(T_s, \theta_0)$:

$$k(T_s, \theta_0) = (1 - 3\theta_0) \left[k_m(T_s, \theta_0) - \theta_0 \frac{dk(T_s, \theta)}{d\theta} \Big|_{\theta_0} \right]. \quad (10)$$

The derivative of the rate constant cannot be determined independently from the rate constant itself, but Eq. (10) can be used to fit a set of $k_m(T_s, \theta_0)$ measured at different T_s and θ_0 to an arbitrary functional form for $k(T_s, \theta_0)$.

So, assuming that we know the coverage dependence of the sticking coefficient, we still must acquire a large number of rate measurements over a wide coverage range to fit the coverage dependence of $k_m(T, \theta_0)$ to a proposed coverage dependent form of $k(T_s, \theta_0)$. However, we do not need any measurements of incident beam flux densities.

III. FOURIER ANALYSIS: MEASURING RATES AND LINEARIZATION OF KINETICS

We utilized discrete Fourier analysis to extract the first-order rate constants, k_m , from our measured modulated coverage and modulated CO desorption flux waveforms. The advantages to this method include the ability to easily deconvolute instrument and time-of-flight (TOF) contributions from our measurements and the ability to quickly and easily

assess whether or not the kinetics have been linearized. The deconvolution process has been described well by Brown and Sibener,²⁵ and we only note here that our incident beam TOF distributions were measured directly, and we assume the same thermal TOF distributions that Brown did.

Sawin²⁶ has shown that the mapping of the complex Fourier components of a waveform to the complex plane can be used to characterize the underlying kinetics. For our system, the discrete Fourier transform of Eq. (4) is expressed in terms of the discrete components for $\Delta\theta(t)$, $\Delta\theta_j$, and $I(t)$, I_j ,

$$\begin{aligned} -i \sum_{j=0}^{2^n} \omega_j \Delta\theta_j \exp(-i\omega_j t) \\ = S \sum_{j=0}^{2^n} I_j \exp(-i\omega_j t) - k_m \sum_{j=0}^{2^n} \Delta\theta_j \exp(-i\omega_j t), \end{aligned} \quad (11)$$

where $\omega_j = 2\pi j/2\tau$. The transform for $I(t)$ contains no even components (j even), so the remaining odd harmonics (j odd) are used to determine the rate constant. Solving Eq. (11) for the individual components:

$$-i\omega_j \Delta\theta_j = SI_j - k_m \Delta\theta_j. \quad (12)$$

In practice we normalize $I(t)$ and $\Delta\theta(t)$, so $S = I_0 = \theta_0 = 1$. By solving Eq. (12) for $\Delta\theta_j$ and dividing $\Delta\theta_j$ by I_j , we solve for the kinetic response function P_j :

$$P_j = \frac{\Delta\theta_j}{I_j} = \frac{k_m + i\omega_j}{k_m^2 + \omega_j^2} = \text{Re}(P_j) + i\text{Im}(P_j). \quad (13)$$

We recover k_m by noting that $k_m = \omega_j \text{Re}(P_j)/\text{Im}(P_j)$, using the $j = 1$ components, since they are least sensitive to high frequency noise in the data.

We used the transform to characterize the linearization by first noting that a linearized rate should result in a single exponential response in the response function P_j , which has a semicircular shape in the complex Fourier plane. We illustrate this with the simulated waveforms shown in Fig. 2. As the modulation amplitude is increased for waveforms with an exponentially increasing rate constant with coverage in Fig. 2(a), the increasingly nonlinear response is reflected in the shape of the transfer function in Fig. 2(c). Equation (8) predicts that, if I_W is not small enough, the rate constant will change in the middle of the modulation period, resulting in an asymmetric response function as reflected by the increase in the amplitude of the $j = 2$ harmonic in Fig. 2(b).

Problems can arise if the modulation period is too short for the measured rate constant. This is illustrated with simulated waveforms in Fig. 3. In practice, the transform is carried out by subtracting a base line from each discrete point in the waveform and then applying a fast Fourier transform (FFT) routine to the normalized modulated part of the signal [Fig. 3(a)]. An explicit solution and subsequent transform of the kinetic response function reveals that, if the modulation period is not long enough with respect to k_m , the odd components produced this traditional way will not fall on the semicircle; however, the explicit solution also produces a correction factor $c = [1 + \exp(-k_m \tau)]/[1 - \exp(-k_m \tau)]$ that when divided into each real and imaginary odd component, will put the truly first order com-

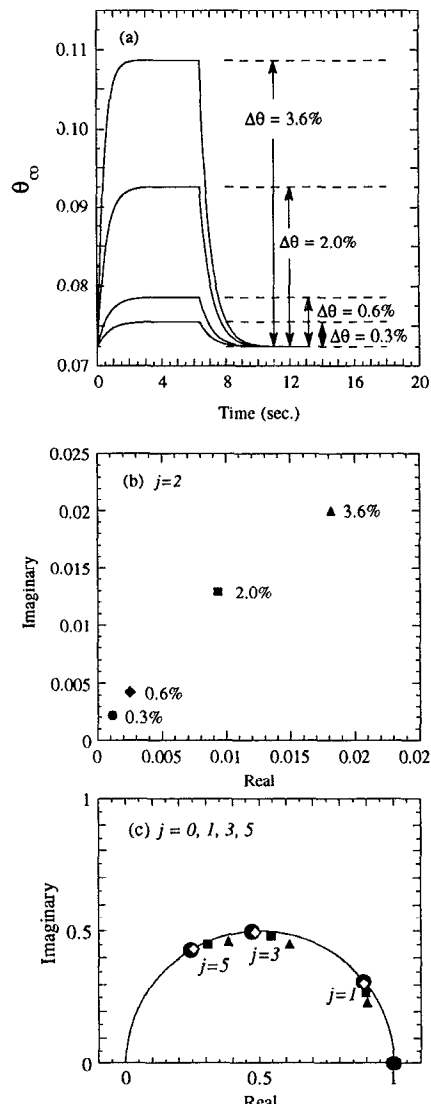


FIG. 2. Here we demonstrate the problem of overmodulation. (a) Four simulated waveforms at increasing modulation amplitude for the experimentally determined desorption rates at the indicated coverages and $T_s = 490$ K. Analysis of these waveforms shows the corresponding increasing deviations of the $j = 2$ harmonic from zero (b) as well as deviations of the odd harmonics from a semicircle (c). The calculated rate constants for the 0.3% (circle), 0.6% (diamond), 2.0% (square), and 3.6% (triangle) are 1.41 , 1.44 , 1.64 , and 1.92 s^{-1} , respectively.

ponents on the semicircle [see arrows in Fig. 3(b)]. With these corrections, the transform was used to calculate rate constants and assess whether or not those rate constants were truly first order rate constants.

IV. EXPERIMENTAL

The apparatus, described elsewhere,^{25,27} consists of a three molecular-beam source, an ultrahigh vacuum (UHV) chamber with rotatable quadrupole mass spectrometer, and the controlling computer system. The molecular-beam source contains three quadruply differentially pumped molecular beams horizontally coplanar and aligned and collimated to a single scattering center in the UHV chamber. Each beam has a computer-controlled beam shutter, and the

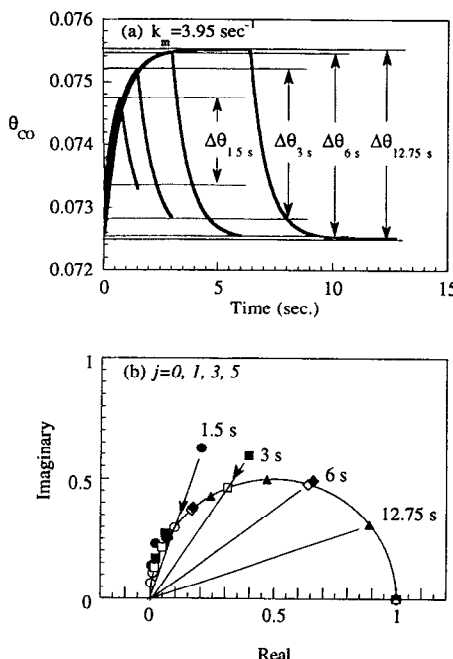


FIG. 3. For a given $k_m = 3.95 \text{ s}^{-1}$, reducing the modulation period 2τ will result in reduced modulation amplitudes $\Delta\theta_{2\tau}$ for simulated perfect first-order waveforms (a). Since only the modulated part of the waveform is Fourier transformed, if $k_m < \omega_1$ ($\omega_1 = \pi/\tau$), the resulting $j = 1, 3, 5$ harmonics (filled symbols) will incorrectly indicate nonlinear kinetics, although an accurate first order rate constant is obtained from the data. By dividing the real and imaginary coefficient by the correction factor $c = [1 + \exp(-k_m\tau)]/[1 - \exp(-k_m\tau)]$, the odd harmonics will correctly indicate whether or not the rate is a first-order rate (open symbols). Both uncorrected and corrected $j = 1$ harmonics can be used to calculate k_m , which is proportional to the ratio of the real to imaginary part of the $j = 1$ harmonic (solid lines).

center He beam has a 10–400 Hz chopper 21.21 cm from the scattering center. The intensities of the two CO side beams, axially 15° from the center beam, were varied either by raising and lowering the backing pressure or by using two mixtures, 20% and 90%, of CO in He. The UHV chamber contained the Rh(111) crystal, oriented to within 0.5°, on a fully rotatable mount which also allowed for 140° azimuthal rotation and tilting of the crystal about the scattering plane.

The UHV chamber, pumped with a 400 l/s ion pump, also contains an Auger-sputter gun assembly that is moved under the crystal for argon ion sputtering and Auger spectroscopy. The quadrupole mass spectrometer, with electron bombardment ionizer 14.45 cm from the scattering center, is rotatable from –5° to 135° from the three-beam plane. The crystal is rotatable from –135° to 135° from the three-beam plane.

The computer system, an AST 286 interfaced to a computer-aided measurement and control (CAMAC) crate and a Eurotherm temperature controller, was used to control shutter timing, temperature, and mass spectrometer rotation as well as to collect kinetics, TPD, reflectivity, and diffraction data. The product waveforms were collected with 2" ($n = 6, 7, 8, 9$, or 10) channels.

Surface preparation consisted of heating the Rh(111) crystal in 10^{-5} Torr O₂ for 2–3 h at 500–900 K, sputtering in

5×10^{-5} Torr of argon at 3 μA for 1.5–2 h at 500–900 K, and annealing to 1300 K. Cleanliness was checked with Auger, and cleaning procedures were repeated until S, C, and B, the only detectable contaminants, were no longer detectable. The magnitude of the He reflectivity was also used to check the surface quality. The Debye-Waller factor, β , is given by

$$I_{\text{He}_{\infty}}(T_S) = I_{\text{He}_{\infty}}(T_S = 0) \exp(-\beta T_S), \quad (14)$$

where $I_{\text{He}_{\infty}}(T_S = 0)$ is the zero coverage He intensity at 0 K and $I_{\text{He}_{\infty}}(T_S)$ is the reflected zero coverage He intensity at T_S . β was determined by temperature dependent He reflectivity measurements each day varying between 0.0030 and 0.0032 for the room temperature (63 meV) 45° incident He beam. The surface temperature was maintained and measured to within 0.1 K with the Eurotherm temperature controller. The day to day consistency of β was used to indicate surface cleanliness, and values of $I_{\text{He}_{\infty}}(T_S)$ extrapolated from these high temperature measurements were used when $I_{\text{He}_{\infty}}(T_S)$ could not be directly measured due to adsorption of background CO at lower surface temperatures (e.g., $T_S < 600$ K).

The crystal was cooled for diffraction and low temperature kinetics measurements via a liquid nitrogen cold finger electrically insulated from the resistive heating system controlled by the Eurotherm. Typically, in order to maintain 1300 K, we required a current of 40 A. For diffraction, the crystal was azimuthally oriented along the $\langle 01\bar{1} \rangle$ and $\langle 11\bar{2} \rangle$ directions to within 0.5° using H₂ diffraction. Since the surface layer is hexagonally symmetric, with the symmetry broken only by the second layer, there are six azimuthal orientations which produce H₂ diffraction peaks at the same θ_f (for $\theta_i = 45^\circ$), but at different intensities. Throughout our He diffraction measurements, we always chose the crystal orientation which produced the most intense H₂ diffraction peaks. All He diffraction was done with a 45° incident He beam which was produced by supersonic expansion of 40 psig He behind a 100 μ pinhole. The chamber pressure rise due to this beam was typically 3×10^{-9} Torr, and the straight through (unscattered) beam has a full width at half-maximum (FWHM) of 1°. All gases and gas mixtures were purchased from Linde, with the He being ultrahigh purity grade.

V. RESULTS

A. He diffraction

1. (2×2)-CO/Rh(111)

He diffraction measurements were made for a number of CO coverages and surface temperatures in order (i) to characterize the CO overlayer for the CO desorption kinetics measurements and (ii) to measure the approximate order to disorder phase transition temperature. As mentioned, all diffraction was done with a 45° incident room temperature (63 meV) He beam. For the saturated (2×2) CO overlayer, the sharpest He diffraction peaks were obtained by dosing the Rh(111) surface continuously with the highest intensity possible (~1 ML/s) CO beam as the surface was first heated to 600 K, then cooled to $T_S < 170$ K and dosed for 5–10 min more. Diffraction scans along the $\langle 11\bar{2} \rangle$ [Fig. 4(a)]

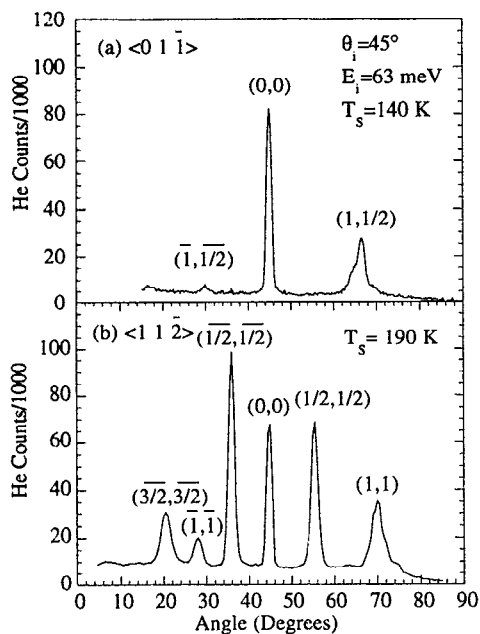


FIG. 4. Shown are He diffraction curves for a $\theta_i = 45^\circ$, $E_i = 63$ meV helium beam scattered along the $\langle 0\ 1\ \bar{1} \rangle$ azimuth at 140 K (a) and the $\langle 1\ 1\ \bar{2} \rangle$ (b) azimuth at 190 K. Peak positions agree well with those expected from the established (2×2) -CO/Rh(111) 0.75 monolayer ordered overlayer.

and $\langle 0\ 1\ \bar{1} \rangle$ [Fig. 4(b)] azimuths were consistent with the (2×2) -CO overlayer. The diffraction peaks disappear rapidly if the surface is heated to ~ 260 K, or ~ 285 K if the surface is continuously dosed with ~ 1 ML/s of CO. Castner and Somorjai¹⁹ note that the (2×2) LEED pattern is produced at 300 K only by raising the CO pressure to 1×10^{-5} Torr. Comparisons of relative CO coverages measured with TPD confirm that the disappearance of the (2×2) overlayer occurs when CO desorbs.

2. $(\sqrt{3}\times\sqrt{3})R30^\circ$ -CO/Rh(111)

The $(\sqrt{3}\times\sqrt{3})R30^\circ$ overlayer was also studied with He diffraction. Two overlayer growth procedures were used which produced optimal $(\sqrt{3}\times\sqrt{3})R30^\circ$ structures. In one procedure we dosed the crystal with an excess of CO (~ 200 L) at $T_s = 380$ K and then cooled the crystal without further dosing. CO in excess of $\frac{1}{3}$ ML quickly desorbed at 380 K while coverages of $\frac{1}{3}$ ML and less remain constant over many minutes at that temperature. In a second procedure we produced comparable overlayers by heating a (2×2) overlayer to 380 K. Heating the sample any higher would result in a loss of the diffraction peak due to, as confirmed by TPD measurements, partial desorption of the overlayer.

He diffraction scans for the $(\sqrt{3}\times\sqrt{3})R30^\circ$ overlayer, taken as the crystal was first heated then cooled, reveal that the diffraction peaks, including the specular (0,0) peak, decrease in intensity and ultimately disappear around 325 K (Fig. 5). There was no measurable change in the diffraction peak widths. The subsequent reappearance of the specular peak at higher temperatures is believed to be specular diffraction or reflection from the Rh(111) surface associated with desorption of the overlayer, as will be discussed later. However, unlike the (2×2) overlayer, the $(\sqrt{3}\times\sqrt{3})R30^\circ$

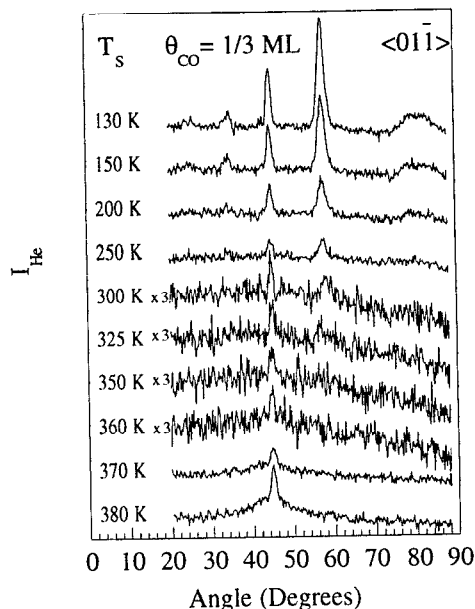


FIG. 5. Shown are He diffraction curves for a $\theta_i = 45^\circ$, $E_i = 63$ meV He beam along the $\langle 0\ 1\ \bar{1} \rangle$ azimuth. At $T_s = 130$ K, peak positions agree well with those expected from the established $(\sqrt{3}\times\sqrt{3})R30^\circ$ CO/Rh(111) $\frac{1}{3}$ ML ordered overlayer, with the (0,0) peak at 45° and the larger $(1/3, 2/3)$ peak at 59° . As the surface temperature is increased, the diffraction pattern disappears until at 325 K no diffraction is visible. At higher temperatures, the specular peak starts to grow, indicating some loss of CO coverage as the helium starts to scatter from the Rh(111) substrate. If the overlayer is heated quickly (in ~ 1 min) to 380 K and immediately cooled back to 130 K, the diffraction pattern is reproduced, demonstrating that a disordered $\frac{1}{3}$ ML phase exists between 325 and 380 K.

overlayer's diffraction peaks disappeared without CO desorbing. Comparison of the desorption intensities for the (2×2) and $(\sqrt{3}\times\sqrt{3})R30^\circ$ show a ratio of 0.42 ± 0.03 , or, assuming that the (2×2) coverage is 0.75 (monolayer), a coverage of 0.32 ± 0.02 for the $(\sqrt{3}\times\sqrt{3})R30^\circ$ overlayer.

Using He reflectivity measurements while dosing with CO to establish and measure lower CO coverages, as will be discussed, we also attempted to observe ordering of lower coverage overlayers. The results, shown in Figs. 6(a) and 6(b), indicate little or no ordering for the 0.09 and 0.18 ML overlayers even at the lowest temperatures accessible. This behavior is characteristic of repulsive nearest-neighbor interactions. There is a broad, unresolved peak centered at specular, presumably due to diffuse scattering from the adsorbate, and the much narrower specular peak from the Rh(111) surface. There is no evidence for ordering or islanding at any measured CO coverage ($\theta_{CO} < \frac{1}{3}$ ML) above 380 K, the temperature at which CO starts to measurably desorb below $\frac{1}{3}$ ML.

B. CO coverage calibration

Having established the relevant relationships between coverage, temperature, and ordering for the CO overlayer, we next established the relationship between coverage and He reflectivity. We define reflectivity as the ratio of specular He intensity at some CO coverage to the intensity for the bare surface at the same temperature. Between 325 and 380 K, where there is no diffraction from the overlayer, there is a

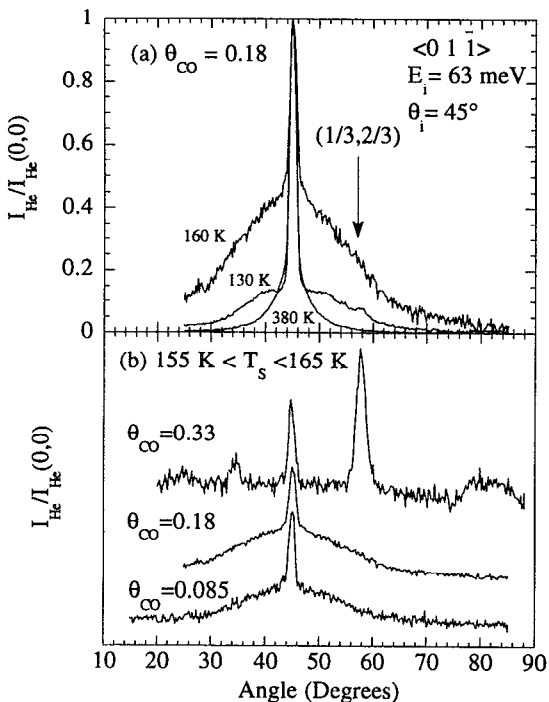


FIG. 6. With scattering conditions the same as in Fig. 7, there is no evidence for helium diffraction from a $\theta_{\text{CO}} = 0.18$ ML CO/Rh(111) overlayer from above 380 K until perhaps 130 K, where a small shoulder is seen in the diffraction signal (a). As coverage is decreased from $\frac{1}{3}$ to 0.085 over a small temperature range around 160 K (b), there is, again, no evidence for ordering at coverages below $\frac{1}{3}$ of a monolayer.

monotonic relationship (Fig. 7) between specular intensity and CO exposure or, equivalently, CO coverage, since CO does not desorb significantly in this temperature range. Since we extrapolate this relationship to higher temperatures where CO desorption rates are significant, we note that there is no evidence for a temperature dependence of specular He scattering vs coverage. We can therefore unambiguously

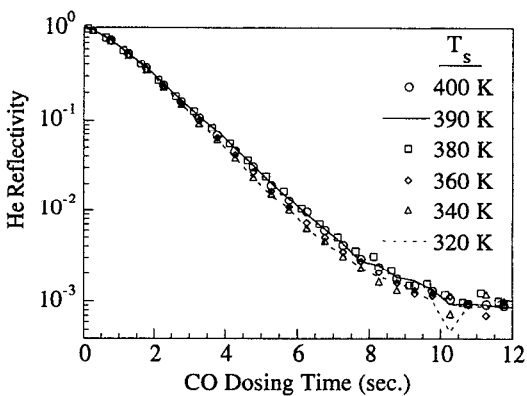


FIG. 7. He reflectivity (specular helium intensity divided by zero coverage specular helium intensity) is plotted as a function of CO dosing time at six different surface temperatures within the disordered regime. Since there is no significant CO desorption over the 12 s dosing period at the indicated surface temperatures, the CO coverage increases at the same rate for all indicated T_s . The close agreement between all of the attenuation curves indicates that there is little temperature dependence in the relationship between helium reflectivity and CO coverage for the disordered CO overlayer.

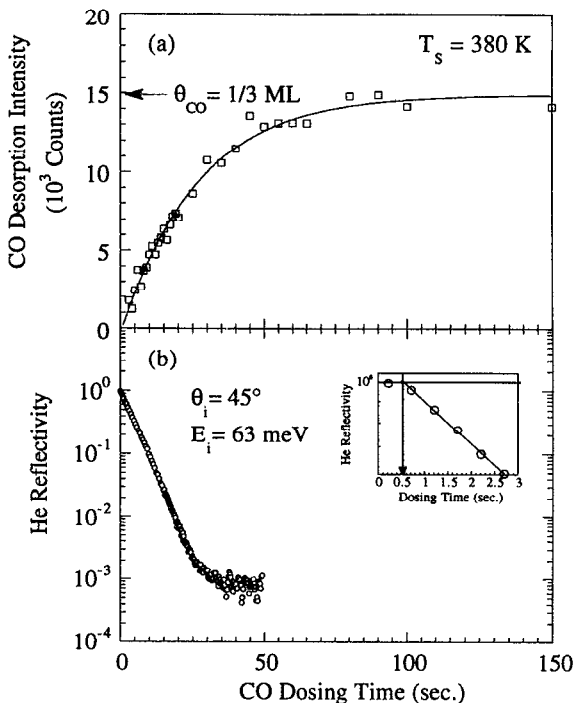


FIG. 8. Helium reflectivity is calibrated against CO coverage by monitoring helium reflectivity for a CO adsorption isotherm. The CO coverage for a set of constant CO flux density exposure or dosing times onto 380 K Rh(111) is determined by the CO intensity for a flash desorption [squares (a)]. From previous measurements, the terminal coverage is $\frac{1}{3}$. The sticking behavior fits Langmuir adsorption kinetics (solid line) $d\theta/dt = S_0 I_{\text{CO}} (1 - 3\theta)$, with $S_0 I_{\text{CO}} = 0.0122 \text{ ML/s}$ and 1 ML = 44 880 counts CO. Helium reflectivity is measured for exposure to the same CO beam flux density (b). The 0.51 s delay before the onset of a nearly linear decrease in the helium reflectivity is shown [(b) inset] and may be due to adsorption at defects or a change in the sticking behavior (see text).

calibrate He reflectivity reliably for coverages up to $\frac{1}{3}$ ML.

The calibration was accomplished by monitoring the He reflectivity during a CO adsorption isotherm. In an effort to keep the crystal clean during calibration, the highest temperature where terminal CO coverage is $\frac{1}{3}$, 380 K, was used. The coverage for the adsorption isotherm was determined by flash desorbing CO from the crystal after each exposure. The integrated intensity for each flash desorption is plotted against dosing (or exposure) time and fitted to a Langmuir adsorption isotherm with $\frac{1}{3}$ ML as the terminal coverage [see Fig. 8(a)], solid curve]. From this fit, we see that the coverage dependent sticking coefficient is well described by Eq. (2). We note that we saw the same type of Langmuir adsorption for both CO-He beam mixtures, indicating that the coverage dependence of the sticking coefficient is independent of our beam velocities ($v_{\text{avg}} = 8.0 \times 10^4$ and $12.0 \times 10^4 \text{ cm/s}$, respectively, for the 90% and 20% CO in He mixtures). Also, the $S_0 (1 - 3\theta)$ form fits the whole adsorption isotherm and is not just the limiting case as $\theta \rightarrow \frac{1}{3}$ ML.

Figure 8(b) shows the attenuation in He reflectivity for a 63 meV, $\theta_i = 45^\circ$ He beam during the same CO beam exposure. There is a 0.51 s delay between the beginning of the CO dosing and the onset of a steady, exponential attenuation of the reflectivity as a function of time [Fig. 8(b), inset]. For systems like the disordered CO overlayer on Rh(111), the

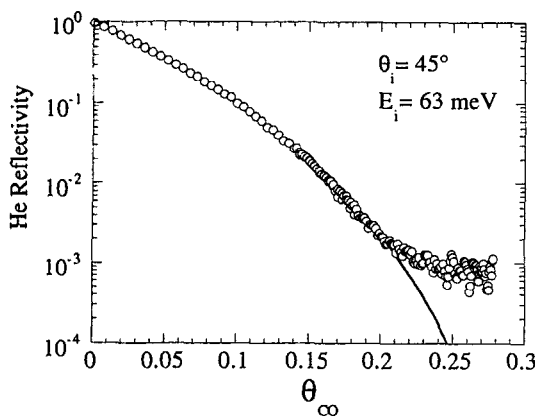


FIG. 9. He reflectivity is plotted as a function of coverage using combined data from Figs. 11(a) and 11(b). The Comsa-Poelsema model (solid line) fits up to 0.22 ML using the following parameters: $\Sigma_{CO} = 148 \text{ \AA}^2$, $\eta = 0.13 \text{ \AA}^{-2}$ (known from rhodium lattice constants), and $m = 3.163$.

He attenuation can be analyzed using a Comsa-Poelsema²⁸ model for adsorbates with repulsive nearest-neighbor interactions (see Fig. 9, solid curve):

$$\frac{I_{He}}{I_{He_{\infty}}} = (1 - m\theta_{CO})^{\Sigma_{CO}\eta/m}, \quad (15)$$

where $\Sigma_{CO} = 148 \text{ \AA}^2$ is the best-fit value for the He-CO scattering cross section (Fig. 10), $\eta = 0.13 \text{ \AA}^{-2}$ is the known Rh(111) surface atom density, and $m = 3.163$ is the best-fit value for θ_{CO}^{-1} at saturation. Although this model is useful for understanding the origin of the attenuation, the coverages in this paper come from the calibration data, not the model.

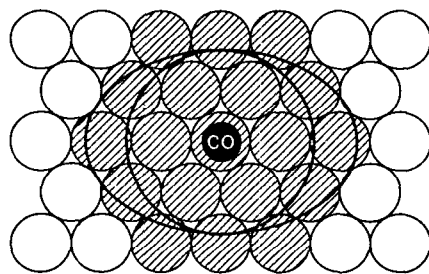
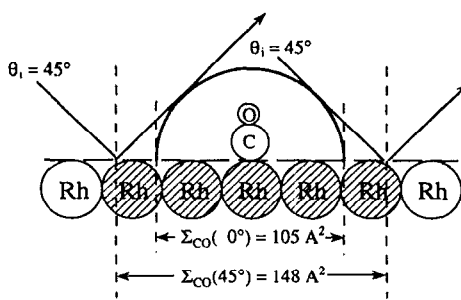


FIG. 10. This figure, adapted from Ref. 28, indicates that the origin of the large attenuation cross-section CO has for specular He scattering is due to the long range attractive part of the He-CO/Rh(111) potential. The Comsa-Poelsema model predicts a $\cos^{-1}(\theta_i)$ dependence for the cross section, which predicts a 104 \AA^2 cross section for a 0° incident helium beam.

The 0.51 s delay may be due to adsorbed CO filling in defect sites before filling in top sites; CO at defect sites on Pt(111) has a 42 \AA^2 cross section compared with 123 \AA^2 for CO on top sites.²⁸ Assuming that, initially, CO sticks and migrates to defect sites, an upper limit to the defect density is 0.006, and, from the initial slope of the He attenuation, a lower limit on the scattering cross section for CO at defects is $\sim 20 \text{ \AA}^2$. All coverages quoted are coverages in addition to defect adsorption.

Another possible explanation for this delay is that, as Menzel notes,¹ $S = S_0(1 - 7\theta)$ as $\theta \rightarrow 0$ for adsorption systems with nearest-neighbor repulsive interactions. Assuming the initial cross section is 148 \AA^2 , the initial slope of the adsorption isotherm comes within 10% of the predicted sticking behavior, with the behavior "switching" to $S_0(1 - 3\theta)$ at $\theta_{CO} = 0.006$.

The sticking coefficient reveals much about the nature of the basic interactions between adsorbates. As noted above, the $S = S_0(1 - 7\theta)$ form for the sticking coefficient results from nearest-neighbor repulsions because adsorption is excluded not only from the adsorption site itself [as with $S = S_0(1 - \theta)$], but also for the six surrounding sites. The $S = S_0(1 - 3\theta)$ form reveals that the average number of unoccupied nearest-neighbor sites per occupied site is 2, the smallest number possible for adsorbates with no nearest-neighbor occupancies. As noted, we observe this form for the sticking coefficient for the lowest coverages we have studied.

C. CO desorption kinetics

1. Direct CO desorption

Near-zero coverage kinetic measurements were made by directly measuring desorbing CO. The incident angle for the CO beam was 45° , and the desorbed CO was collected at 0° (crystal normal). We measured rates for coverages up to 0.003 (ML) and rate constants from 60 to 3000 s^{-1} over a temperature range from 580 to 650 K . Beam modulation times (2τ) were from 6 to 100 ms. With these low coverage measurements, the desorbed CO flux density is proportional to CO coverage, and $k = k_m$. The rate constant is extracted by deconvoluting both the incident square wave function and the CO TOF function from the waveform.²⁵ Incident CO TOF's were measured directly, and crystal to detector TOF's were assumed to be thermal.²⁵ Figure 11 shows the Arrhenius plot for this data and a typical waveform. The activation energy was 32.8 kcal/mol , and the pre-exponential was $2.54 \times 10^{14} \text{ s}^{-1}$.

2. He reflectivity

The CO desorption kinetics measurements made with He reflectivity ranged in coverage from <0.003 to 0.219 ML , with k_m ranging from 0.35 to 25 s^{-1} over a temperature range of 440 – 555 K . Beam modulation periods were from 1 to 40 s. Data were collected by first selecting a specific reflectivity, which corresponded to a specific adsorbate coverage, at a selected surface temperature. The continuous (intense) beam flux was adjusted by raising or lowering the backing pressure until this reflectivity was achieved. Next the modulated (low intensity) beam flux was adjusted until, at low

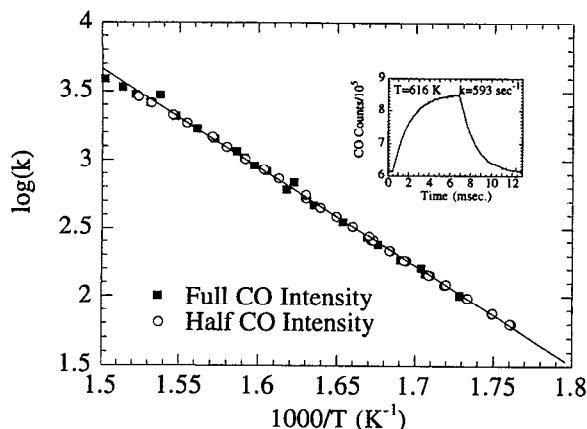


FIG. 11. Shown is an Arrhenius plot of desorption data taken in the high temperature limit for extremely low coverage. Rate constants were measured using conventional waveform analysis of the CO desorption flux (in contrast to He reflectivity measurements). Measurements were made at two incident beam intensities differing by approximately a factor of 2. Both data sets fit an Arrhenius model with parameters $v_0 = 2.54 \times 10^{14} \text{ s}^{-1}$ and $E_a = 32.8 \text{ kcal/mol}$. A typical waveform is shown in the inset.

coverages, the weak beam induced a 5%–10% drop per modulation cycle in He reflectivity, and, at high coverages, a 20%–30% drop in reflectivity. This corresponds to a 0.2%–0.8% (ML) modulation in CO coverage (Fig. 12).

The waveforms were analyzed by first converting the reflectivity change upon adsorption and desorption to a coverage response [$-\ln(I/I_0)$] is linear for small coverage

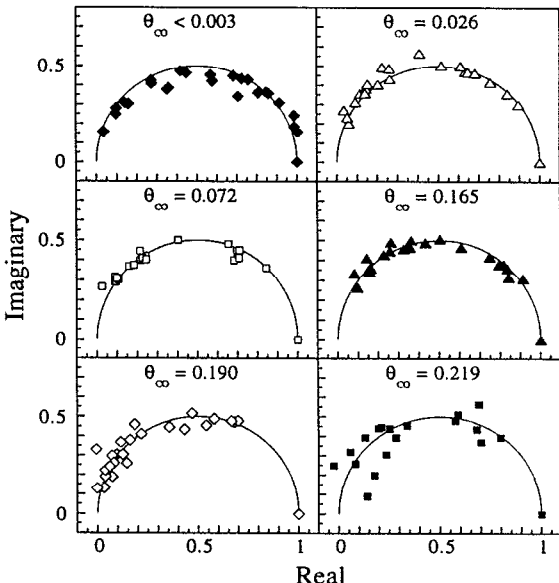
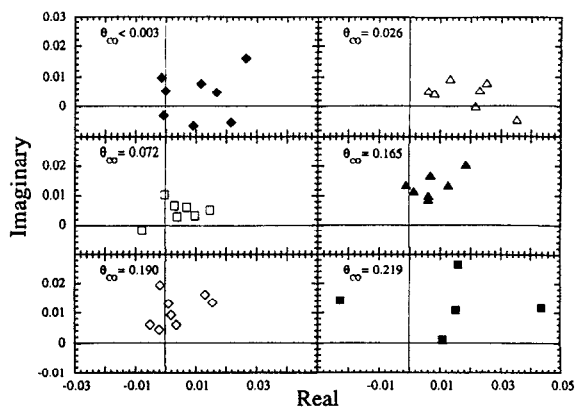


FIG. 13. Fourier analysis of all waveforms indicates whether kinetic responses are symmetric (a) [see Fig. 2(b)] and linear (b) [see Fig. 2(c)]. Waveforms that did not look symmetric or linear from this analysis were scrutinized further and discarded if they were, indeed, not symmetric or nonlinear.

changes] and transforming the waveform. The $j = 2$ harmonic was used to check the symmetry of each waveform [Fig. 13(a)], and the $j = 0, 1, 3$, and 5 harmonics were used to check the linearity of each waveform [Fig. 13(b)]. Although our simulated waveforms (see Fig. 2) suggest that the asymmetry and nonlinearity of the waveforms are coupled, there are examples of kinetic mechanisms, such as diffusion limited kinetics, for which the resulting waveform is symmetric but the response function is nonlinear. Also, there exists the possibility of a compensation between the two halves of a waveform that produces a linear response function for an asymmetric waveform. We therefore must check for both symmetry and linearity. Since noise and timing errors can lead to transform errors, all waveforms whose transforms seemed nonlinear or asymmetric were checked and the data discarded if the waveforms turned out to actually be nonlinear or asymmetric. The $j = 1$ harmonic was then used to determine k_m from the remaining good waveforms.

$k_0(T_S)$, the zero coverage rate constants, are equal to $k_m(T_S, \theta = 0)$. From an Arrhenius plot (Fig. 14, $\theta_{CO} = 0$),

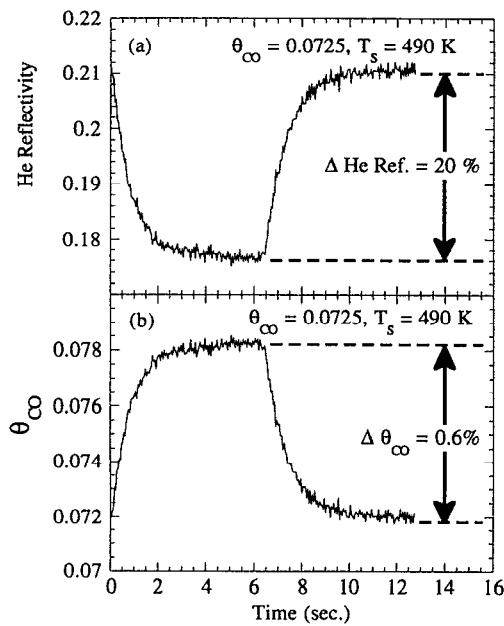


FIG. 12. This figure clearly demonstrates the remarkable “kinetic response amplification” properties that time-resolved specular He reflectivity has for measuring surface kinetics. Coverage dependent kinetic data is collected by measuring the change in helium reflectivity as a function of CO modulation time (a). From the reflectivity vs coverage calibration (see Fig. 12), the reflectivity response is converted to a coverage response (b) with, in this case, a 20% modulation in helium reflectivity corresponding to a 0.6% modulation in overall coverage. From the base line of the waveform the steady state coverage $\theta_0 = 0.72$ is determined. Analysis of the CO coverage waveform yields a measured rate constant $k_m = 1.16 \text{ s}^{-1}$.

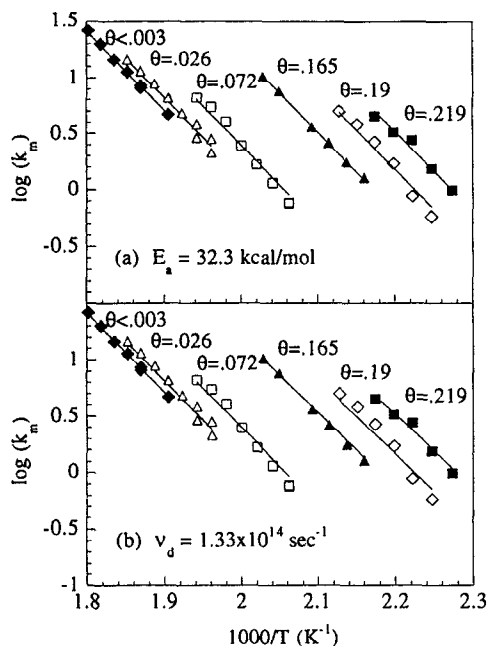


FIG. 14. Shown are isosteric Arrhenius plots for measured CO desorption rates (k_m). Measured rate constants are grouped such that θ_0 was within 0.5% of the indicated coverage, except for $\theta_0 = 0.190$. Due to changing detector sensitivity, the upper four data points for $\theta_0 = 0.190$ are at a slightly different coverage from the lower two data points. Solid lines are best fits to the data for $k(\theta, T)$, the actual CO desorption rates, assuming that (a) only v_d changes with coverage or (b) only E_a changes with coverage.

$v_d = 1.33 \times 10^{14} \text{ s}^{-1}$ and $E_a = 32.3 \text{ kcal/mol}$. We note that the experimental conditions for these lower temperature, near-zero coverage measurements produce higher coverage modulations than for our higher temperature, near-zero coverage measurements. Although defects can dramatically alter desorption rates as coverages approach zero,⁵ these measured rates agree well with the higher temperature desorption rates from Sec. V C 1.

Ideally, for a surface reaction one should be able to linearize the kinetics such that k_m is the reaction rate for all coverages. For desorption, as shown in Eq. (8), the coverage responds not only to the desorption rate but also to the change in rate and the change in sticking coefficient as a function of coverage. Questioning the necessity of including these terms, i.e., are these terms inherently coupled to the desorption rate, we intentionally analyzed the data without accounting for these factors. We found that the exclusion of either of the derivative terms in Eq. (8) will yield rate constants that, using Eq. (4), do not reproduce the waveforms,

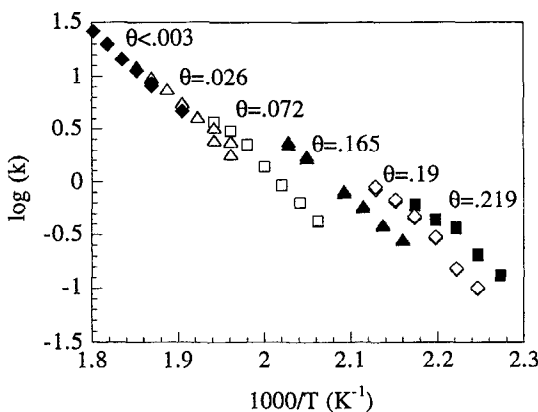


FIG. 15. Shown is an Arrhenius plot of the desorption rate constants $k(\theta, T_S)$ calculated from the measured rate constants assuming either constant v_d or constant E_a [see Figs. 17(a) and 17(b)]. We note no significant differences in the resulting rate constants.

our original data. We therefore conclude that the derivative terms in Eq. (8) must be included in the kinetic analysis of experiments in which the overall change in coverage is measured.

With the measured $k_m(\theta, T_S)$ [Figs. 14(a) and 14(b)], we could use either Eqs. (7) or (10) to determine $k(\theta, T_S)$. Beam intensities were not routinely measured. We therefore analyze the rate constants first with Eq. (10). This approach requires that we first choose a form for the coverage dependence of $k(\theta, T_S)$ and check that the form is self-consistent with Eq. (10). Assuming an Arrhenius form for the coverage dependent rate constant, $k(\theta, T_S) = v_d(\theta) \exp[-E(\theta)/k_b T_S]$, we tried several forms for $v_d(\theta)$ and $E(\theta)$.

Pfnür, Feuler, and Menzel² saw an almost constant quasi-equilibrium E_a for CO on Ru(001) for coverages from 0 to 0.25, with a change of almost two orders of magnitude for v_d . Assuming here that only v_d changes with coverage, the data is isostERICALLY fit to $E_a = 32.3 \text{ kcal/mol}$ [Fig. 14(a)]. We find that

$$v_d(\theta) = 1.33 \times 10^{14} \exp(0.344\theta + 48.8\theta^2) \text{ s}^{-1}. \quad (16)$$

If we assume that $v_d = 1.33 \times 10^{14}$ for all coverages, then we find from the isosteric data [Fig. 14(b)] that

$$E(\theta) = 32.3 - 1.62\theta - 38.3\theta^2 \text{ kcal/mol}. \quad (17)$$

Table I summarizes the Arrhenius parameters for each measured coverage as predicted by each of the assumed forms for the rate constants. If we apply Eq. (10) to each individual rate constant for any of the assumed forms for the rate constant, we see in Fig. 15 that there is no distinct difference for the predicted rates. We note that a triangular lattice-lattice gas approach by Leüthäuser²⁹ fits our data well for a repulsive nearest-neighbor interaction energy $\epsilon = 2.52 \text{ kcal/mol}$, but his assumption of a coverage independent sticking coefficient is physically unreasonable for our system. In general, though, the fact that desorption rates increase with increasing coverage is a strong indication of repulsive nearest-neighbor interactions, which result in a decrease in total adsorption energy with increasing adsorbate coverage.

TABLE I. Coverage dependent Arrhenius parameters.

θ_{CO}	E_a (kcal/mol)	v_0 (s^{-1})	E_a (kcal/mol)	v_0 (s^{-1})
0.000	32.3	1.33×10^{14}	32.30	1.33×10^{14}
0.026	32.3	1.39×10^{14}	32.23	1.33×10^{14}
0.072	32.3	1.76×10^{14}	31.98	1.33×10^{14}
0.165	32.3	5.32×10^{14}	30.98	1.33×10^{14}
0.190	32.3	8.27×10^{14}	30.61	1.33×10^{14}
0.219	32.3	1.49×10^{15}	30.11	1.33×10^{14}

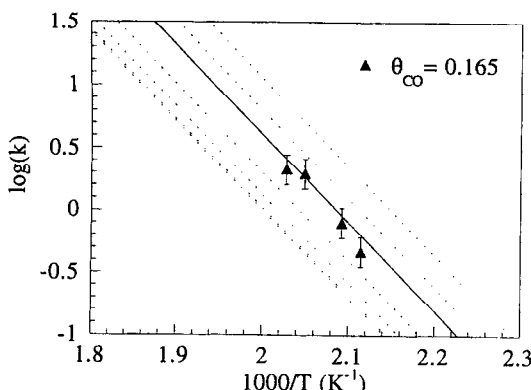


FIG. 16. In this figure, the relationship $k(\theta, T_s) = k_m(I_s/I_w)[\Delta\theta(r)/\theta_0]$ is used to extract rate constants for $\theta_0 = 0.165$ (triangles), which are compared with rates for $\theta_0 = 0.165$ predicted from Fig. 17(a) (solid line) as well as rates for other measured coverages (dotted lines).

Another way to check our rates is to apply the other rate measurement methods, which require fewer assumptions to extract rates. Although we could not measure incident CO flux densities with precision (this problem has since been corrected by installing ion-gauge fluxmeters), we used two methods to indirectly measure flux densities. The first method utilizes our measurements of the near-zero coverage rate constants and the steady state equation at near-zero co-

verage, $S_0 I = k_0(T)\theta$. For each incident flux density, I , we adjusted the crystal temperature until we saw a 5% drop in He reflectivity, corresponding to a CO coverage of 0.0027. Since we knew $k_0(T)$ at each temperature, we readily determined $S_0 I$ for a range from 0.052 to 0.6 ML/s. Note that the measurement combines the beam velocity dependence of S_0 and the flux density into a single measurement. With intensities determined by this method, we apply Eq. (7) to $\theta_{CO} = 0.163$ ML data (Fig. 16), for which we have reasonably accurate values for I_w as well as k_m , I_s , $\Delta\theta$, and θ_0 .

With values for I_s from the first method, as well as values from a second method for which we scattered CO from a 600 K crystal and collect the desorbed flux at normal, we applied Eq. (3). We determined quasi-equilibrium rate constants ($T_{gas} \neq T_s$) for $\theta_{CO} = 0.026, 0.072, 0.115, 0.165, 0.190$, and 0.219 at several surface temperatures [Figs. 17(a) and 17(b)]. We compare these new rate constants to those predicted by Eq. (16) and find that all three methods produce rates that are in good agreement, indicating that all our assumptions about sticking coefficients and the forms for the rate constants were valid.

VI. DISCUSSION

A. Thermodynamic approach

At equilibrium, the coverage dependent desorption rate constants can be expressed as a coverage dependent chemical potential which, in turn, can be related directly to the interaction energies of CO on the surface. Equilibrium between the gas phase and the adsorbed phase can be characterized by two different equations, one thermodynamic, the other kinetic. The thermodynamic equation equates the adsorbate chemical potential, μ_a , to the gas phase chemical potential, μ_g :³⁰

$$\mu_a = \mu_g = E_g + k_b T \ln p \left(\frac{h^2}{2\pi m k_b T} \right)^{3/2} \frac{1}{k_b T} \frac{1}{f_r f_v} \quad (18)$$

with E_g the ground state energy for the gas phase, p the pressure, T the gas and surface temperature, and f_r and f_v the rotational and vibrational partition functions for gas phase molecules. The kinetic equation, basically a restatement of Eq. (1) for an equilibrium gas, states that the rate of adsorption equals the rate of desorption:

$$s(\theta, T) \frac{p}{N_s (2\pi m k_b T)^{1/2}} = k(\theta, T) \theta \quad (19)$$

with N_s the density of rhodium atoms on the surface and $s(\theta, T)$ the sticking coefficient for an equilibrium gas phase sample.

By combining these two equations, we arrive at a relationship between the measured quasi-equilibrium desorption rate and the adsorbate chemical potential:

$$k(\theta, T) = s(\theta, T) f_r f_v \frac{k_b T}{h^3} \frac{2\pi m k_b T}{\theta N_s} \exp\left(\frac{\mu_a - E_g}{k_b T}\right). \quad (20)$$

At the limit of zero coverage, where there is no interaction between adsorbates, the adsorbate chemical potential approaches the Langmuir lattice gas limit:

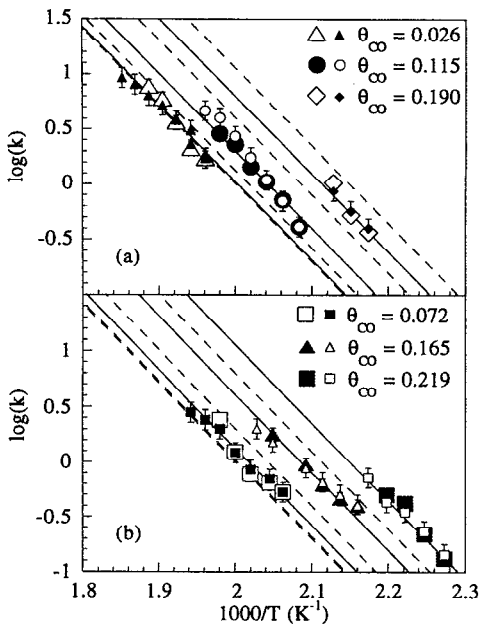


FIG. 17. In this figure, the relationship $k(\theta, T_s) = S_0(1 - 3\theta)I_s/\theta_0$ is used to extract rate constants for $\theta_0 = 0.026, 0.115$, and 0.190, as indicated, in (a) and $\theta_0 = 0.072, 0.165$, and 0.219, as indicated, in (b). These rate constants are compared to rates predicted from Fig. 17(a) for these coverages, with solid lines for the indicated coverages and dashed lines otherwise. Since two different methods were used to determine I_s (see text), the resulting calculated rates are differentiated by larger symbols for I_s from isosteric desorption rate measurements and smaller symbols for I_s from direct desorption flux measurements.

$$k(\theta, T) = \frac{\theta}{1-\theta} s(\theta, T) f_r f_v \frac{k_b T}{h^3} \frac{2\pi m k_b T}{\theta N_s} \times \exp\left(\frac{E_a - E_g}{k_b T}\right) \quad (21)$$

for which E_a is the energy for each adsorption site. Assuming $s_0 = 1$, $f_r = T/(2.77 \text{ K})$, and $f_v = 1$ this lattice gas model predicts $\nu_0 = 6 \times 10^{17} \text{ s}^{-1}$ at 500 K and a T^3 temperature dependence for ν_0 . Although the temperature range for our data is too small to determine the exact temperature dependence for ν_0 , ν_0 is several orders of magnitude smaller than the model prediction, implying that either S_0 is several orders of magnitude smaller or that more terms must be added to the adsorbate partition function. Since the only measurements of S_0 place it between 0.5³¹ and 1,¹⁶ we conclude that the adsorbates have more degrees of freedom than predicted by the Langmuir lattice gas model.

The two-dimensional (2D) gas model,¹⁷ given by

$$k(\theta, T) = \frac{\theta}{1-\theta} s(\theta, T) f_r f_v \frac{k_b T}{h} \frac{1}{AN_s \theta} \exp\left(\frac{E_a - E_g}{k_b T}\right) \quad (22)$$

with A the hard-core area per adsorbate, allows for a much higher entropy for the adsorbed gas. This model predicts $\nu_0 = 7 \times 10^{14} \text{ s}^{-1}$ at 500 K (assuming the ratio of the area of a rhodium atom to a CO molecule at the surface, AN_s , is 3). If we further consider the effects of low frequency frustrated rotational degrees of freedom³² on this value, we find a further reduction of ν_0 . For example, using two frustrated rotations at 30 meV yields $\nu_0 = 3 \times 10^{14} \text{ s}^{-1}$. We note that the temperature dependence of ν_0 is T^2 in the 2D gas model, but is independent of T in the Arrhenius formulation. We could not explore this temperature dependence due to the small temperature range of our measurements.

Since our objective was to determine the coverage dependence of the desorption rate, we relate the coverage dependent rate to the zero coverage rate

$$k(\theta, T) = s(\theta, T) \frac{k_0(T)}{s_0(T)\theta} \lambda_{a'}(\theta, T), \quad (23)$$

where $\lambda_{a'}(\theta, T)_{\lim \theta \rightarrow 0} = \theta$ and is equivalent to the activity for the adsorbed molecules normalized to the activity at zero coverage for each temperature T . This approach leads directly to an additive form for the coverage dependence of the chemical potential:

$$\mu_a(\theta, T) = \mu_0(T) + \mu_{a'}(\theta, T), \quad (24)$$

where

$$\mu_0(T) = E_g + k_b T \ln \frac{h^3}{k_b T} \frac{N_s}{2\pi m k_b T} \frac{k_0(T)}{s_0(T)} \frac{1}{f_r f_v} \quad (25)$$

is the zero coverage chemical potential minus the coverage dependent term and

$$\mu_{a'} = k_b T \ln [\lambda_{a'}(\theta, T)] \quad (26)$$

is the coverage dependent part of the chemical potential that represents the contribution from the adsorbate partition function and adsorbate interaction energies.

Ibach *et al.*³⁰ point out that several approaches to for-

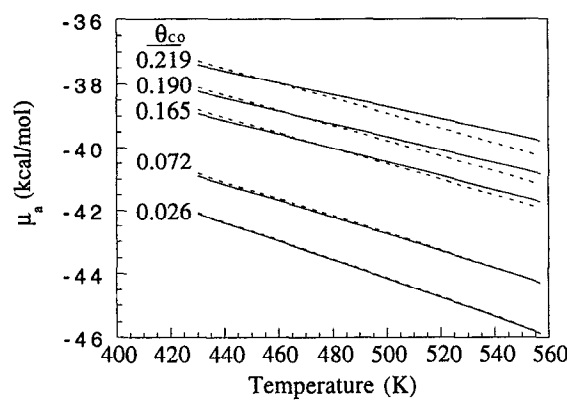


FIG. 18. Shown are isosteric chemical potentials calculated from the experimental rate measurements as a function of temperature assuming constant E_a (solid line) or constant ν_d (dotted line). The coverages, from bottom to top, are 0.026, 0.072, 0.165, 0.190, and 0.219. The measured sticking coefficient, $S(\theta) = 1 - 3\theta$, was used in this calculation.

mulating a chemical potential based on repulsive interactions between adsorbates can lead to a λ_a term that may assign the coverage dependence to the effective activation energy or pre-exponential. Our results reflect this and, in fact, there is no apparent difference between assigning the coverage dependence to the activation energy or the pre-exponential. The Leüthäuser²⁹ formulation illustrates an example for which coverage affects both the effective activation energy (although weakly) and the effective pre-exponential. Using Eqs. (16) or (17), we can formulate $\mu_{a'}$ as either

$$\mu_{a'} = k_b T \{ \ln [s_0(T)\theta / s(\theta, T)] + 0.344\theta + 48.8\theta^2 \} \text{ kcal/mol} \quad (27)$$

or

$$\mu_{a'} = k_b T \ln [s_0(T)\theta / s(\theta, T)] + 1.62\theta + 38.3\theta^2 \text{ kcal/mol.} \quad (28)$$

These equations can be related back to a virial expansion of the chemical potential [see Eq. (2) of Ref. 14] by Taylor expansion of $\ln [s_0(T)/s(\theta, T)]$ in powers of T and θ , once $s(\theta, T)$ and $s_0(T)$ are known. We note that expansion of the chemical potential to include only first-order coverage terms in Eq. (27) or (28) will not describe our data. Expansion to higher than second-order coverage terms does not significantly improve the description of our data, and neither does expansion with both temperature dependent and temperature independent first and second order coverage terms.

Values for $\mu_a(\theta, T)$ based on the temperature independent form for the sticking coefficients, $s_0(1 - 3\theta)$, and the two forms for the chemical potential from Eqs. (27) and (28) are presented in Fig. 18.

B. Adsorption sites: Bridge versus top

In determining how to describe the adsorbate interactions, there are two important aspects of the adsorbates to consider. One is the type of site that the adsorbate sits on, which determines both the fundamental adsorbate energy and what types of interactions are likely at higher coverages.

The other is the ordering of the adsorbate on the surface, which determines with how many adsorbates a particular adsorbate interacts. Clearly there are at least two regimes for CO desorption. The low temperature desorption regime, as noted, is a compressed, mixed phase. There is strong evidence from EELS work¹⁷ that, starting with a compressed (2×2) overlayer, which contains both bridge bonded and top bonded CO adsorption sites, heating the surface to 370 K causes desorption leading to only top bonded molecules.

The high temperature desorption regime, which we concentrated on, consists of CO primarily on top sites. The EELS spectra presented in Fig. 5 of Ref. 17 [taken with Rh(111) in 1×10^{-5} Torr CO] show no evidence for bridge bonded species at $T_s = 530$ K and above. Applying our measured adsorption and desorption rates for these conditions to estimate coverages, we conclude that there is no bridge bonded species below 0.1 ML and below 530 K. Since the He scattering cross section Σ_{CO} and coverage factor m are constant up to 0.22 ML (see Fig. 9), we conclude that the same relative nearest-neighbor spacing of CO to CO persists up to 0.22 ML at 380 K even with an incident CO flux. Migration to bridge sites at higher temperatures (up to 530 K) and coverages ($0.1 < \theta < 0.22$) seems unlikely since the total number of repulsive interactions between top and bridge species is even greater than at $\theta = 0.1$ ML. These results strongly indicate that up to 0.22 ML, for our experimental conditions, virtually all sites populated are top sites.

C. Application to reactions

One of the primary objectives of this experiment was to determine how to routinely measure adsorbate coverages and coverage dependent kinetics with He scattering for the simple case of a single adsorbate. With this accomplished, we can use the knowledge gained from such measurements to further study the coverage dependence of reaction mechanisms, including the determination of energy disposal pathways³³ as a function of adsorbate density.

In this paper we observed the effect of increasing the CO coverage on CO desorption kinetics. It is reasonable to expect that repulsive CO–CO interactions will lead to similar effects on the kinetics of the CO oxidation reaction. Zhdanov, for example, has presented lattice-gas models for both desorption¹¹ and reactions³⁴ that have similar terms for the dependence of the kinetic rates on coverage and interaction energies. Also, Kang *et al.* have recently explored the effect of interadsorbate interactions on reaction rates.¹⁵

We have recently carried out preliminary experiments which confirm the utility of conducting concurrent He specular scattering and reactive scattering measurements. Here CO oxidation rates were measured in the limit of high oxygen coverage.²³ Time-resolved specular He reflectivities were used during reactive scattering to probe adsorbate coverage, modulation depth, overlayer structure, and reaction kinetics. We have therefore demonstrated the feasibility of extending the techniques presented in this paper to study coverage dependent heterogeneous reactions.

VII. SUMMARY AND CONCLUSIONS

(1) Measurements of the coverage dependent desorption rates of CO from Rh(111) have been made utilizing

time-resolved specular He scattering to amplify small coverage changes for isothermal, nearly isosteric conditions and allow linearization of kinetics.

(2) Three different ways of determining the desorption rate constant from the CO coverage data were explored. Each led to almost identical rate constants for the desorbing CO.

(3) For the modulated coverage measurements, the measured rate consists of derivative terms for the sticking coefficient and the desorption rate constant in addition to the actual desorption rate. These additional terms are significant and must be included in the kinetic analysis.

(4) The CO sticking coefficient has a $(1 - 3\theta)$ coverage dependence.

(5) The CO overlayer is disordered for all conditions for which kinetics were measured. He diffraction peaks for the $\frac{1}{3}$ ML ($\sqrt{3} \times \sqrt{3}$) R30° overlayer decrease steadily as the crystal is heated and disappear entirely at 325 K.

(6) He reflectivity attenuates monotonically with CO coverage for the disordered overlayer below $\frac{1}{3}$ ML. The Comsa-Poelsema equation, consistent with nearest-neighbor repulsive interactions, predicts the relationship between attenuation and coverage well for coverages from 0 to 0.22 ML, with a cross section for a room temperature 45° incident He beam of 148 Å² and a saturation coverage of $\frac{1}{3}$ ML.

(7) For temperatures from 450 to 550 K and CO coverages from > 0.003 to 0.22, the CO desorption kinetics are described equally well by

$$k(\theta, T_s) = 1.33 \times 10^{14} \exp[0.344\theta + 48.8\theta^2 - (32.3 \text{ kcal/mol})/(k_b T_s)] \text{ s}^{-1}$$

or

$$k(\theta, T_s) = 1.33 \times 10^{14} \exp[-(32.3 - 1.62\theta - 38.3\theta^2 \text{ kcal/mol})/(k_b T_s)] \text{ s}^{-1}.$$

Desorption rates which increase with increasing coverage are consistent with nearest-neighbor repulsive interactions. A Monte Carlo approach that accounts for the observed coverage dependent rates will be presented in a forthcoming paper.³⁵

(8) A Langmuir lattice gas formula does not accurately predict the near-zero coverage desorption rates and predicts rates that are three orders of magnitude too high. A 2D gas model with two low energy (30 meV) frustrated rotational modes predicts rates well.

(9) Coverage dependent chemical potentials are calculated from the kinetics data. The coverage dependence of the rates can be explained equivalently by a second-order expansion of chemical potential that is either temperature dependent, as shown above, or temperature independent, corresponding directly to a coverage dependent desorption energy.

(10) The time-resolved helium reflectivity techniques described in this paper are applicable to studies of surface reactions as well as simple desorption, thus allowing investigation of density dependent effects in surface chemical reactions.

ACKNOWLEDGMENTS

The authors thank Kevin Gibson and Jennifer Colonell for useful discussions and technical assistance. We also thank H. J. Kreuzer and R. Gomer for their helpful suggestions and discussions. This work was supported in part by the Office of Naval Research and by the NSF Materials Research Laboratory program at The University of Chicago.

- ¹H. Pfnür and D. Menzel, *J. Chem. Phys.* **79**, 2400 (1983).
- ²H. Pfnür and D. Menzel, *J. Chem. Phys.* **79**, 4613 (1983).
- ³For a review, see, M. P. D'Evelyn and R. J. Madix, *Surf. Sci. Rep.* **3**, 413 (1984).
- ⁴B. J. Hinch and L. H. Dubois, *Chem. Phys. Lett.* **171**, 131 (1990).
- ⁵C. T. Rettner, D. S. Bethune, and E. K. Schweizer, *J. Chem. Phys.* **92**, 1442 (1990).
- ⁶L. D. Peterson and S. D. Kevan, *Surf. Sci. Lett.* **235**, L285 (1990).
- ⁷E. W. Scharpf and J. B. Benziger, *Langmuir* (submitted).
- ⁸For a review, see, E. G. Seebauer, A. C. F. Kong, and L. D. Schmidt, *Surf. Sci.* **193**, 417 (1988).
- ⁹Y. B. Zhao and R. Gomer, *Surf. Sci.* **239**, 189 (1990).
- ¹⁰B. Poelsema, R. L. Palmer, and G. Comsa, *Surf. Sci.* **136**, 1 (1984).
- ¹¹V. P. Zhandov, *Surf. Sci. Lett.* **111**, L662 (1981).
- ¹²S. H. Payne, H. J. Kreuzer, and L. D. Roelofs, *Surf. Sci.* (in press).
- ¹³J. B. Benziger and G. R. Schoofs, *J. Phys. Chem.* **88**, 4439 (1984).
- ¹⁴L. D. Peterson and S. D. Kevan, *Phys. Rev. Lett.* **65**, 2563 (1990).
- ¹⁵H. C. Kang, T. A. Jachimowski, and W. H. Weinberg, *J. Chem. Phys.* **93**, 1418 (1990).
- ¹⁶P. A. Thiel, E. D. Williams, J. T. Yates Jr., and W. H. Weinberg, *Surf. Sci.* **84**, 54 (1979).
- ¹⁷L. H. Dubois and G. A. Somorjai, *Surf. Sci.* **91**, 514 (1980).
- ¹⁸M. A. Van Hove, R. J. Koestner, J. C. Frost, and G. A. Somorjai, *Surf. Sci.* **107**, 439 (1981).
- ¹⁹D. G. Castner and G. A. Somorjai, *Surf. Sci.* **83**, 60 (1979).
- ²⁰M. A. Van Hove, R. J. Koestner, J. C. Frost, and G. A. Somorjai, *Surf. Sci.* **129**, 482 (1983).
- ²¹D. F. Padowitz and S. J. Sibener, *J. Vac. Sci. Technol. A* **9**, 2289 (1991).
- ²²D. F. Padowitz and S. J. Sibener, *Surf. Sci.* **254**, 125 (1991).
- ²³D. F. Padowitz, K. A. Peterlinz, and S. J. Sibener, *Langmuir* (in press).
- ²⁴B. Poelsema and G. Comsa, *Faraday Discuss. Chem. Soc.* **80**, 247 (1985).
- ²⁵L. S. Brown and S. J. Sibener, *J. Chem. Phys.* **89**, 1163 (1988).
- ²⁶H. H. Sawin and R. P. Merrill, *J. Vac. Sci. Technol. A* **19**, 40 (1981); H. H. Sawin, Ph.D. dissertation, University of California, Berkeley, May, 1980.
- ²⁷K. D. Gibson and S. J. Sibener, *J. Chem. Phys.* **88**, 791 (1988).
- ²⁸B. Poelsema and G. Comsa, *Scattering of Thermal Energy Atoms from Disordered Surfaces* (Springer, New York, 1989).
- ²⁹U. Leitthäuser, *Z. Phys. B* **37**, 65 (1980).
- ³⁰H. Ibach, W. Erley, and H. Wagner, *Surf. Sci.* **92**, 29 (1980).
- ³¹S. Oh, G. B. Fisher, J. E. Carpenter, and D. W. Goodman, *J. Catal.* **100**, 360 (1986).
- ³²J. S. Ha and S. J. Sibener, *Surf. Sci.* (in press).
- ³³L. S. Brown and S. J. Sibener, *J. Chem. Phys.* **90**, 2807 (1989).
- ³⁴V. P. Zhdanov, *Surf. Sci. Lett.* **102**, L35 (1981).
- ³⁵C. Uebing, K. A. Peterlinz, T. J. Curtiss, and S. J. Sibener (to be submitted).